The International Journal of Advanced Manufacturing Technology (2021) 116:3339–3353
https://doi.org/10.1007/s00170-021-07616-z

ORIGINAL ARTICLE

On-line autonomous path optimization for multi-pass incremental forming using model predictive control

An He[1] · Chenhao Wang[1] · Sheng Liu[1] · Paul A. Meehan[1]

Received: 20 October 2020 / Accepted: 28 June 2021 / Published online: 20 July 2021

Abstract
Model predictive control (MPC) is an advanced control algorithm that has been successfully implemented in the on-line path optimization of computer-numerical-control (CNC) machines for performing single-pass incremental sheet forming (ISF) processes, aiming at precision enhancements of products. Multi-pass ISF technique is usually employed to manufacture parts with extremely large wall angles which cannot be achieved without failure using the single-pass ISF. However, existing studies show that the geometric precision of the products of multi-pass ISF is usually very poor, which has significantly hampered the widespread application of this technique in industry. In the present study, two control algorithms based on the MPC framework were proposed, targeting at achieving a more precise geometry of multi-pass ISF products. MPC-1 was an extension of the control algorithm for the single-pass ISF process reported in our previous work, and MPC-2 was developed for the first time. The developed MPCs were comparatively validated by a group of physical benchmark test. Compared to MPC-1, MPC-2 reduced the maximum geometric error in the wall, conjunction, and base zones on the same part by 26%, 51%, and 73%, respectively. The test results show that MPC-2 had a better performance in multi-pass ISF processes.

Keywords Model predictive control · Path optimization · Multi-pass incremental forming

1 Introduction

In recent years, market demands of small-batch customized production have been raised [1]. In sheet manufacturing industries, these demands were mainly reflected in forming parts with customized geometries. Conventional sheet manufacturing approaches, such as stamping and deep-drawing, are performed with geometry-specific dies. Customized production with conventional approaches is not practicable, since making the dies for each specific part requires high time and economic cost. However, in single-point incremental sheet forming (ISF) process, an infinite variety of parts can be manufactured from flat sheets without using part-specific dies by a mobile tool controlled by a robot [2–4] or a computer-numerical-control (CNC) machine [5–7]. This great flexibility makes single-point ISF a potential rapid and low-cost solution to customized sheet forming [8, 9].

In the process of manufacturing a flat sheet to a part with a specific geometry by ISF, the surface area of the sheet increases, which leads to the thinning of thickness of the sheet, according to the volume conservation theory [5]. The thickness of the part decreases as the wall angle increases, which is usually approximated by the sine law [10]. Therefore, when manufacturing parts with large wall angles by single-point ISF, cracks are likely to occur due to excessive thinning [6, 11]. This significantly limits the variety of the parts that can be successfully formed by ISF. To breakthrough this formability limitation, researchers have proposed various multi-pass ISF approaches. Unlike a typical ISF process in which a part was formed in one pass, in the multi-pass ISF process, several intermediate shapes were pre-formed in the intermediate passes before the final shape was formed. With the multi-pass approaches, a variety of parts which were unable to be formed by the typical one-pass ISF processes were achieved without failure, including an "ellipsoidal cup"–shaped part and a "clover cup"–shaped part by Kim and Young [12]; parts with vertical walls by Duflou et al. [10], Skjoedt et al. [13],

✉ An He
an.he@uq.net.au

[1] School of Mechanical & Mining Engineering, The University of Queensland, Brisbane, Queensland 4072, Australia

and Liu et al. [14]; and a car taillight bracket by Junchao et al. [15].

Besides the formability limitation, poor geometric accuracy of the product, i.e., large dimensional deviation between the formed and the target parts, is another factor that has been hampering the widespread use of ISF in manufacturing industries [1, 7, 16]. Using the parts formed by ISF that cannot meet the geometric requirements may significantly lower the performance and the service life of machines. In ISF processes, parts are formed through accumulations of localized deformations around the end of the tool [11, 16]. Therefore, the tool path is a key factor that determines the geometries of formed parts and may be optimized to achieve higher geometric accuracies. To this end, researchers have proposed various off-line or on-line tool path optimization approaches. Off-line optimization means the tool path was updated after forming a part completely based on the measurement of geometric error, including a proportional tool path adjustment method proposed by Hirt et al. [17], a Fourier and wavelet transforms-based tool path corrections method proposed by Fu et al. [18], and artificial cognitive systems developed by Fiorentino et al. [19, 20]. By the reported off-line optimization approaches, tool paths were adjusted iteratively until the desired geometric accuracies were reached, which meant forming the whole parts physically or numerically for multiple times was required.

To avoid the high time and economic costs of the iterative forming processes, other researchers proposed on-line autonomous tool path optimization approaches, including model predictive control (MPC). The MPC approach uses an optimizer to solve the desired control decision, based on a prediction model that characterizes the input and output of the system under control [21]. In the ISF process, the MPC approach was applied at each sampling instant to autonomously optimize the subsequent tool path, using the measurement of the geometry of the partially formed part. Hao and Duncan [22] reported a linear MPC algorithm for single-point ISF for the first time and significantly enhanced the geometric accuracies of a cone-shaped part and a pyramid-shaped part. In their work [22], the geometry responses were measured in open-loop tests prior to the closed-loop processes. The measurement of geometry responses had to be re-conducted if the target part changed, which made the generalization of this control algorithm difficult. To develop a more generalized MPC approach for ISF, Lu et al. [7, 23, 24] proposed an analytical geometry prediction model based on the geometric abstraction of the target parts. This prediction model was firstly applied in an MPC algorithm for optimizing the vertical increments of the tool paths of single-point ISF processes and greatly reduced the geometric errors on the bases of a cone-shaped part and a pyramid-shaped part [7]. However, on the side walls, the geometric errors remained relatively higher [7]. To improve the geometric accuracies on the side walls, this method was adapted to an MPC algorithm that separately optimized the vertical and radial tool path increments of single-point and multi-point ISF processes [23, 24]. The algorithm developed by Lu et al. [23, 24] was developed using a polar-based frame of reference, and thus the horizontal movement of the tool was fixed in the radial direction. This made the algorithm dysfunctional when forming parts with horizontal contours far away from circular, since the geometric errors were no longer in the radial directions. To solve this problem, He et al. [16] proposed an MPC algorithm with a contour-based frame of reference, which was applicable in forming parts with general horizontal contours. In their work [16], a dog bone-shaped part with a non-convex horizontal contour that was far from circular was successfully formed with a desired geometric accuracy. Later, He et al. [25] further generalized the MPC-based online tool path control approach by developing a switched MPC algorithm which was able to handle parts with varying wall angles.

The multi-pass approach was proved effective in avoiding sheet failure by improving strain distribution, and thus parts with large wall angles could be formed [6, 14]. However, the achieved geometric precisions of the products were usually very poor or unreliable, the improvement of which was of great necessity. To this end, an autonomous on-line tool path optimization approach for multi-pass ISF processes was proposed in this study for the first time. More specifically, two MPC algorithms were formulated. MPC-1 was extended from the MPC algorithm for single-pass ISF processes reported in our previous work [25], which targeted at compensating the geometric errors during all the passes of the multi-pass process and treated each pass independently. MPC-1 was composed of a horizontal control module and a vertical control module. MPC-2 was newly proposed, targeting at compensating the geometric errors raised in the entire process in the final pass, based on the geometries formed in the intermediate passes. MPC-2 consisted of a horizontal control module and a fine control module. A benchmark test was conducted to compare the applicability and the performances of the two MPCs. The generality of the controller was further validated in two additional tests.

2 Methodology

In this section, the methodology of this study will be presented. Parameterizations of the tool path and the geometry will be discussed in sections 2.1 and 2.2. Two model predictive path control algorithms will be presented in sections 2.3 and 2.4, respectively. Experimental methodology will be explained in section 2.5.

2.1 Control variables

As in most cases, z-level tool path was used in this study. Following our previous study [16, 25], the multi-pass ISF was regarded as a discrete-time system, with the tool moving along a closed path at a fixed depth as a sampling instance. The multi-pass ISF process was then split into successive forming steps. The tool path of step k in pass i was parameterized as a periodic spline $\boldsymbol{c}_k^{(i)}$ in the horizontal plane and a depth $z_k^{(i)}$ in the vertical direction. A set of ($\boldsymbol{c}_k^{(i)}$, $z_k^{(i)}$) represented a series of ordered points in the three-dimensional space which formed the tool path, as shown in Fig. 1. To determine the tool path of a step, since the previous step was completed with the tool path known, the horizontal increment $\Delta\boldsymbol{c}$ and the vertical increment Δz of the tool path were chosen as the control variables. For the step k, the horizontal and the vertical tool path increments corresponding to the previous step k-1 were denoted as the step-over $\boldsymbol{u}_{\mathrm{h},\,k}$ and the step-down $u_{\mathrm{v},\,k}$ respectively. The geometric error of the part could be decomposed into the horizontal error and the vertical error, as shown in Fig. 1. The horizontal error and the vertical error were determined by the step-over $\boldsymbol{u}_{\mathrm{h}}$ and step-down u_{v} respectively, and optimizing the step-over $\boldsymbol{u}_{\mathrm{h}}$ and step-down u_{v} was able to reduce the geometric error globally [16, 25].

2.2 Geometry representative points

The measurement of the geometry of the (partially) formed part was a cloud of points. To reduce the computational cost, vertical and horizontal geometry representative points on the formed part were selected to represent the entire part, and their positions in the three-dimensional space quantified the status of the formed geometry. In this study, the method of choosing vertical geometry representative points was the same as reported in our previous study [25]; however, the method for the horizontal geometry representative points was different. Hence, in this section, the method of choosing horizontal geometry representative points was discussed, and the method for the vertical geometry representative points can be referred to [25].

Critical points were selected on the horizontal contour of the edge of the target part, based on the geometric feature. Accordingly, critical sections were made along the normal of the critical points. The target parts in the validation tests of this study had a circular and an elliptical contour, and the critical sections of the parts are shown in Fig. 2. Following our previous study [16, 25], the contour-based local reference frame was used. Detailed explanations of the critical section and the contour-based local reference frame can be found in [16, 25]. In each critical section, as the deformation localized to the area around the end of the tool, the global deformation in the other area was ignored. Besides, since the tool with a round end was used in this study, the formed geometry in the critical section around the end of the tool was an arc. However, this arc geometrically differed with the straight wall of the target part in each intermediate step. Therefore, in order to feed the appropriate geometric information in the horizontal direction back to the controller, only the area where the deformation localized was chosen as the measurement window, as shown in Fig. 2. Horizontal geometry representative points of each step were located in the measurement window of the critical sections in the formed geometry. Tuning variables Λ_{A} and Λ_{B} were introduced to represent the ratio of the depths of the upper and lower boundaries of the measurement window to the target depth. Λ_{A} and Λ_{B} determine the measurement window. For the part with the straight wall, the tuning variables Λ_{A} and Λ_{B} were set as

$$\Lambda_{\mathrm{A}} = \frac{|d_N| - r(1-\cos\alpha)}{|d_N|} \tag{1}$$

$$\Lambda_{\mathrm{B}} = \frac{\left(\widetilde{a} - \widetilde{b}\tan\alpha\right) - \sqrt{\left(\widetilde{b}\tan\alpha - \widetilde{a}\right)^2 - \left[1 + (\tan\alpha)^2\right]\left(\widetilde{a}^2 + \widetilde{b}^2 - r^2\right)}}{\left[1 + (\tan\alpha)^2\right]|d_N|} \tag{2}$$

where

$$\widetilde{a} = \frac{|d_N| - r(1-\cos\alpha)}{\tan\alpha} + r\sin\alpha - \left|\Delta u_{\mathrm{h,max}}\right| \tag{3}$$

$$\widetilde{b} = d_N + r \tag{4}$$

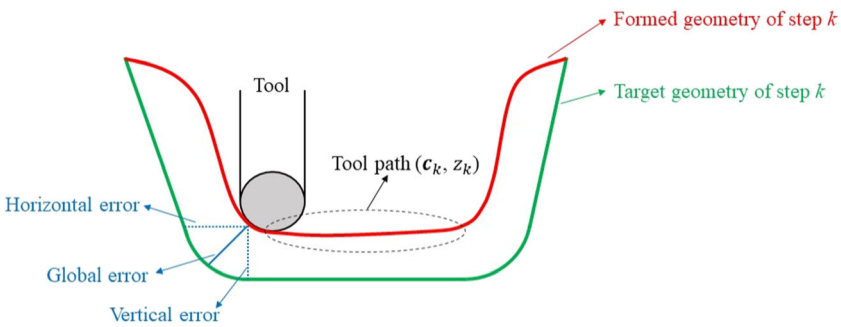

Fig. 1 Illustration of the tool path and the decomposition of the geometric error (representative figure, not to scale).

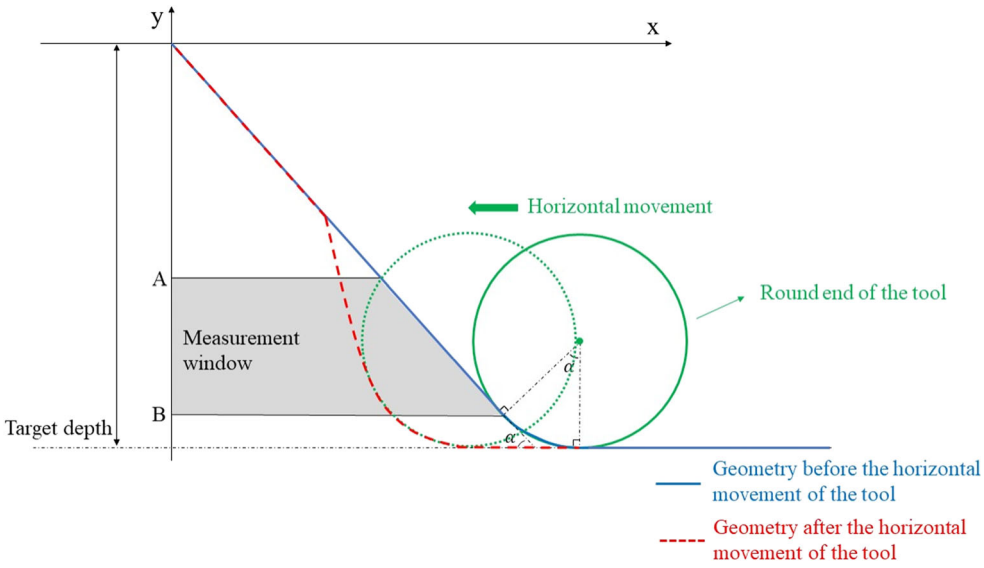

Fig. 2 Vertical section showing of the target geometry and illustration of the measurement window of the horizontal geometric error (representative figure, not to scale).

In the above equations, d_N is the target depth of the part, α is the target wall angle of the part, r is the radius of the end of the tool, and $\Delta u_{\mathrm{h,\ max}}$ is the upper boundary of the optimization of step-overs. The current states of the geometry representative points were the horizontal distances of each point to the edge, while the reference states were the horizontal distances of the horizontal projection points on the target part to the edge. Similarly, the deviation between the current and the reference states was the horizontal error.

It should be noticed that the total number of the horizontal geometry representative points are fixed for all the steps, while that of the vertical geometry representative points varies for different steps. In one step, the vertical geometry representative points are distributed on the entire area surrounded by a closed path $\boldsymbol{c}$, and the locations of the points are determined based on the coordinates in the Cartesian coordinate system. This area changes during the ISF process, and thus the number of the vertical geometry representative points varies for each step. However, the locations of the horizontal geometry representative points are determined based on the ratios of the depths of the points to the target depth, which means the number of the points is independent on the target geometries of each step.

2.3 Model predictive control algorithm 1

In our previous study [25], a MPC algorithm for single-pass ISF processes was developed. In this work, algorithm 1 was developed as an extension of the MPC for the single-pass ISF processes, which was designed to be activated in all the passes of the multi-pass ISF process and treated each pass independently. This algorithm contained a horizontal control module and a vertical control module, which made control decisions of the step-over and the step-down, respectively, aiming at reducing the horizontal and the vertical geometric error when necessary.

For each forming step in each intermediate pass or the final pass, the system can be linearized in both horizontal and the vertical directions and can be expressed with the following state-space model [25]:

$$\boldsymbol{x}^{(i)}_{\Omega,k+1} = \boldsymbol{A}^{(i)}_{\Omega,k+1}\boldsymbol{x}^{(i)}_{\Omega,k} + \boldsymbol{B}^{(i)}_{\Omega,k+1}\boldsymbol{u}^{(i)}_{\Omega,k+1} \tag{5}$$

$$\boldsymbol{y}^{(i)}_{\Omega,k} = \boldsymbol{C}^{(i)}_{\Omega,k}\boldsymbol{x}^{(i)}_{\Omega,k} \quad \forall k = 1,2,3\cdots N_i; \forall i = 1,2,3\cdots \Upsilon \tag{6}$$

where $\boldsymbol{x}$, $\boldsymbol{y}$, and $\boldsymbol{u}$ are the vectors of the state, the system output, and the system input. The superscript i in the bracket represents that the variable is related to the ith pass of the multi-pass ISF process. The subscript k represents that the variable is related to the kth step in the ith pass. The subscript Ω indicates which of the modules the model belongs to and can be $\mathcal{H}$ or $\mathcal{V}$ in this algorithm which represents the horizontal and the vertical modules, respectively. Υ represents the total number of the passes, and N_i represents the total number of steps in the ith pass. In both horizontal and vertical directions, the forming process is assumed to be additive, and thus the coefficient vector $\boldsymbol{A}$ is an identity matrix in both of the two modules. In addition, in all the steps, the states of all the geometry representation points can be directly measured, and thus the coefficient vector $\boldsymbol{C}$ is also an identity matrix in both of the two modules.

In Eqs. (5) and (6), the vector $\boldsymbol{B}$ represents the linear system response, i.e., the geometric change of the part relative to tool perturbations. As the vectors $\boldsymbol{A}$ and $\boldsymbol{C}$ are determined and fixed, the response vector $\boldsymbol{B}$ is the only variable that needs to be solved for the system models. Before determining the response vector $\boldsymbol{B}$, it is presupposed that all types of the geometric errors, including springback and pillow effect, were

handled through the feedback, following our previous study [25]. The geometric response $\boldsymbol{B}$ can be approximated by the nominal geometric response $\overline{\boldsymbol{B}}$ which is the geometric response of the target geometry relative to the nominal tool path.

The vertical module is the same as the vertical modules of the algorithm presented in our previous study [25] and is integrated in this MPC algorithm for multi-pass ISF. The system input $\boldsymbol{u}_{\mathcal{V}}$ is the step-down of the tool path of each step in all the passes. Since the bottom of the target geometry for each step is always a horizontal flat surface, the movements of all the vertical geometry representation points follow the tool path. Therefore, the vertical geometric response $\boldsymbol{B}$ can be obtained:

$$\boldsymbol{B}_{\mathcal{V},k}^{(i)} = \overline{\boldsymbol{B}}_{\mathcal{V},k}^{(i)} = [1 \quad 1 \quad 1 \quad \cdots \quad 1]_{1\times\psi_k^{(i)}}^{T} \quad \forall k = 1,2,3\cdots N_i; \forall i = 1,2,3\cdots\Upsilon \tag{7}$$

where $\psi_k^{(i)}$ is the total number of the vertical geometry representation point in step k of pass i. The detailed discussion about the vertical module can be referred to [25].

To simplify the development of the state-space model for the horizontal module, in each critical section, the contact area between the target geometry and the end of the tool which is an arc shown in Fig. 2 is approximated by line segments, as shown in Fig. 3. The horizontal geometry representative points are evenly distributed within the measurement window determined by the parameters Λ_A and Λ_B. The τth point is taken as an example in the following calculation. A pair of the τth geometry representative points for two neighboring steps k-1 and k is located at the depths of $\phi_\tau d_{k-1}$ and $\phi_\tau d_k$, respectively. ϕ_τ represents the ratio of the depth of the point to the target depth of the corresponding step and ranges from Λ_A to Λ_B. d_{k-1}, and d_k represents the target depth of steps k-1 and k, respectively. It can be seen from Fig. 3 that the lengths of the line segments $\overline{CB}$ and $\overline{BA}$ are the absolute values of the nominal step-over and the nominal step-down, and the length of $\overline{ED}$ is $\phi_\tau|u_{v,k}|$. Triangles FED and CBA are similar, and thus

$$\frac{\overline{FE}}{\overline{CB}} = \frac{\overline{ED}}{\overline{BA}} \tag{8}$$

It can be derived that the length of the line segment $\overline{FE}$ is $\phi_\tau u_{h,k}$. Therefore, the geometric response of the τth geometry representative point in step k can be calculated by

$$b_{\mathcal{H},k,\tau}^{(i)} = \overline{b}_{\mathcal{H},k,\tau}^{(i)} = \frac{\overline{FE}}{\overline{u}_{h,k}} = \phi_\tau \quad \forall\tau = 1,2,3\cdots\chi; \forall k = 1,2,3\cdots N_i; \forall i = 1,2,3\cdots\Upsilon \tag{9}$$

where χ denotes the total number of the points in one critical section. The geometric responses of this point in different steps are fixed. However, for different geometry representative points, the geometric responses are different. Eq. (9) can be used to calculate the geometric responses of all the horizontal geometry representative points within the measurement window, and then the horizontal response vector $\boldsymbol{B}_{\mathcal{H},k}^{(i)}$ can be formulated.

The MPC controller optimizes the trajectories of the step-over and the step-down in a finite prediction horizon. The state-space models, as expressed by Eqs. (5) and (6) for each step in the prediction horizon, are packed into a matrix function. The detailed matrix packing process can be referred to [7]. Therefore, the formed geometries in the prediction horizon can be predicted by

$$\widehat{\boldsymbol{Y}}_{\Omega,k+P|k}^{(i)} = \boldsymbol{Y}_{\Omega,k}^{(i)} + \boldsymbol{B}_{\Omega,k+P|k}^{(i)} \times \widehat{\boldsymbol{U}}_{\Omega,k+P|k}^{(i)} \tag{10}$$

$$\forall k = 1,2,3\cdots N_i; \forall i = 1,2,3\cdots\Upsilon$$

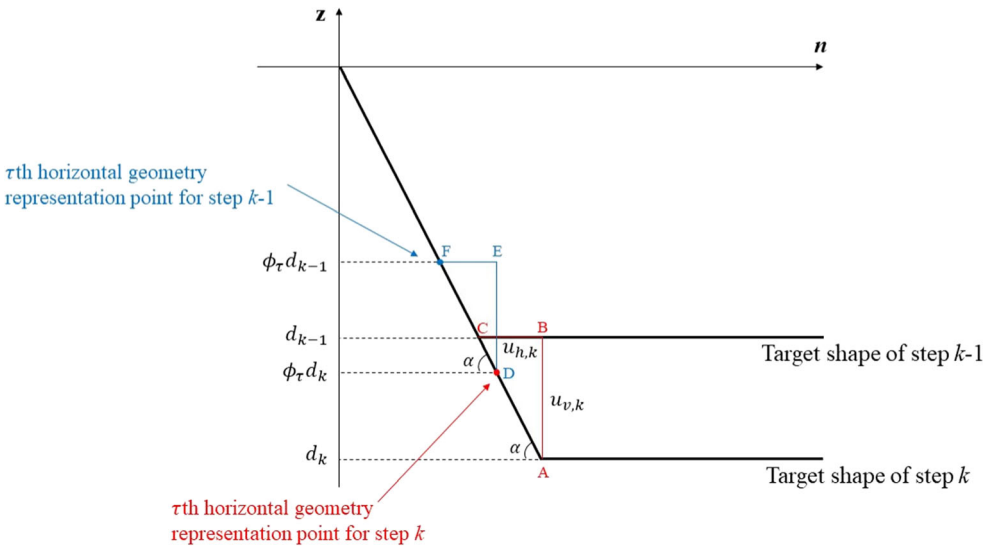

Fig. 3 Simplification of the target geometry in a critical section.

where $\widehat{\boldsymbol{Y}}$ and $\boldsymbol{Y}$ are matrices of the predicted and the currently measured status of the geometry representative points, respectively, and $\widehat{\boldsymbol{U}}$ is the matrix of the predicted step-over or step-down in the prediction horizon. Accordingly, the geometric response matrix $\boldsymbol{B}^{(i)}_{\Omega,k+P|k}$ in the prediction horizon can be formulated as

$$\boldsymbol{B}^{(i)}_{\Omega,k+P|k}=\begin{bmatrix} \boldsymbol{B}^{(i)}_{\Omega,k+1} & \mathbf{0} & \mathbf{0} & \mathbf{0} & \cdots & \mathbf{0} \\ \boldsymbol{B}^{(i)}_{\Omega,k+1} & \boldsymbol{B}^{(i)}_{\Omega,k+2} & \mathbf{0} & \mathbf{0} & \cdots & \mathbf{0} \\ \boldsymbol{B}^{(i)}_{\Omega,k+1} & \boldsymbol{B}^{(i)}_{\Omega,k+2} & \boldsymbol{B}^{(i)}_{\Omega,k+3} & \mathbf{0} & \cdots & \mathbf{0} \\ \vdots & \vdots & \vdots & \vdots & \ddots & \vdots \\ \boldsymbol{B}^{(i)}_{\Omega,k+1} & \boldsymbol{B}^{(i)}_{\Omega,k+2} & \boldsymbol{B}^{(i)}_{\Omega,k+3} & \boldsymbol{B}^{(i)}_{\Omega,k+4} & \cdots & \boldsymbol{B}^{(i)}_{\Omega,k+P} \end{bmatrix}$$

$$\forall k = 1,2,3\cdots N_i; \forall i = 1,2,3\cdots \Upsilon \tag{11}$$

Since the controller aims at finding the optimum solutions of the step-over and the step-down within a reasonable range to reduce the geometric error, the cost function for both modules can be expressed as

$$\boldsymbol{J}^{(i)}_{\Omega,k+P|k} = \left\| \widehat{\boldsymbol{Y}}^{(i)}_{\Omega,k+P|k} - \boldsymbol{W}^{(i)}_{\Omega,k+P|k} \right\|^2_2 + \lambda_\Omega \left\| \boldsymbol{U}^{(i)}_{\Omega,k+P|k} - \overline{\boldsymbol{U}}^{(i)}_{\Omega,k+P|k} \right\|^2_2 \tag{12}$$

$$\forall k = 1,2,3\cdots N_i; \forall i = 1,2,3\cdots \Upsilon$$

where $\boldsymbol{W}$ and $\overline{\boldsymbol{U}}$ are the matrices of the reference states and the nominal step-overs or step-downs in the prediction horizon. λ_Ω is a weighting factor, and the values for the horizontal and the vertical modules are set as 0.7 and 0.2, respectively, following our previous work [25]. The control decision, i.e., the optimized trajectory of step-over or step-down, can be determined through minimizing the cost function. For the horizontal module, the upper and the lower boundaries of the optimization are set as 0.3 and 0.0, respectively; for the vertical module, the boundaries are set as −1.0 and +1.0, respectively. The settings of the optimization boundaries were used in previous experiments with the same equipment and received satisfactory results [25].

In the ISF process, the two modules can be enabled or disabled at any time depending on the design of intermediate shapes. A target part may be successfully formed with various designs of intermediate shapes, and for different designs, the scheduling of the two modules may be different. The detailed implementation of the MPC-1 will be presented in section 2.5.1.

2.4 Model predictive control algorithm 2

The algorithm 2 tries to compensate all the geometric errors raised in the entire multi-pass process in the final pass, based on the geometries formed in the intermediate passes. For the intermediate passes, the nominal tool paths are used. This algorithm is composed of two modules, i.e., a horizontal control module and a fine control module. The horizontal control module is enabled in the nominal forming steps to optimize the trajectory of step-over, so as to reduce the horizontal geometric error. However, as there is no vertical control module in algorithm 2, the nominal trajectory of step-down is used in all the forming steps. Therefore, vertical geometric errors may remain in the bottom of the formed part, which will be compensated by the fine control module. As the horizontal control module integrated in algorithm 2 is the same as that in algorithm 1, in this section, only the fine control module will be discussed.

The nominal tool path of the last step in the first pass can be parameterized as a set of $(\boldsymbol{c}^{(1)}_{N^{(1)}}, z^{(1)}_{N^{(1)}})$. The horizontal element $\boldsymbol{c}^{(1)}_{N^{(1)}}$ is a closed path, inside which is the bottom of the target geometry. According to section 2.2, several vertical geometry representative points are distributed in this area, and the vertical geometric errors for all the points can be measured. If the average of the measured geometric errors is larger than a preset threshold, the fine control module will be enabled. In the final pass, a new forming step will be created to compensate the remaining vertical geometric error. The fine control module works iteratively until the error is small than the threshold. Considering the dimensions of the target parts, which will be presented in section 2.5.1, in this study, the threshold was set as 0.1mm to avoid over-forming.

Since the creation of the new forming step is to compensate the vertical error in the bottom of the formed part, the vertical element z needs to be optimized by the fine control module, while the horizontal element is fixed as $\boldsymbol{c}^{(1)}_{N^{(1)}}$. Step k+1 ($k > N^{(\Upsilon)}$) is taken as an example in the following calculation of the vertical element of the tool path. Suppose the previous step k was formed and the states of the geometry representative points were measured. Based on the linear state-space model expressed by Eqs. (5) and (6), the status of step k+1 can be predicted

$$\widehat{\boldsymbol{Y}}^{(\Upsilon)}_{\mathcal{F},k+1|k} = \boldsymbol{Y}^{(\Upsilon)}_{\mathcal{F},k} + \boldsymbol{B}^{(\Upsilon)}_{\mathcal{F},k+1}\left(z^{(\Upsilon)}_{k+1} - z^{(\Upsilon)}_{k}\right) \quad \forall k = N_\Upsilon, N_\Upsilon+1, N_\Upsilon+2\cdots \tag{13}$$

where the symbol $\mathcal{F}$ in the subscript represents that the variable belongs to the fine control module. As the module works iteratively, the prediction horizon is 1 step. Similar to the vertical control module of the algorithm 1, for each of the geometric representative point in the fine control module, the geometric response $b^{(\Upsilon)}_{\mathcal{F}} = 1$. The cost function is expressed as

$$\boldsymbol{J}^{(\Upsilon)}_{\mathcal{F},k+1|k} = \left\| \widehat{\boldsymbol{Y}}^{(\Upsilon)}_{\mathcal{F},k+1|k} - \boldsymbol{W}^{(\Upsilon)}_{\mathcal{F},N_\Upsilon} \right\|^2_2 \quad \forall k = N_\Upsilon, N_\Upsilon+1, N_\Upsilon+2\cdots \tag{14}$$

Therefore, the vertical element in the tool path of step k+1 can be optimized as

$$z_{k+1}^{*(\Upsilon)} = argmin\ \boldsymbol{J}_{\mathcal{F},k+1|k}^{(\Upsilon)} \quad \forall k = N_\Upsilon, N_\Upsilon + 1, N_\Upsilon + 2\cdots \tag{15}$$

To avoid over-forming, the upper and the lower boundaries for the fine control module are set as 0.0 and −1.0mm respectively. Similar to the algorithm 1, the detailed implementation of the algorithm 2 will be discussed in section 2.5.1.

2.5 Experimental methodology

To test the performances of the developed control algorithms, single-point multi-pass ISF experiments were conducted. Firstly, target geometries are introduced, and the intermediate shapes are determined in section 2.5.1. Then, the detailed implementation of the two algorithms and the experimental apparatus are presented in section 2.5.2.

2.5.1 Target geometries and intermediate shapes

In this study, a circular cone-shaped part and an elliptical cone-shaped part were formed for the validation of the controllers. The horizontal contours of the parts were a circle and an ellipse, respectively. Fig. 4 shows the top views of the two parts along with the dimensions. The wall angles of the two parts were 65°.

The target shape of an intermediate pass is referred to as an intermediate shape. For a multi-pass ISF process, designing of the intermediate shapes is of great importance, which determines whether or not the target part can be formed without failure and the achieved geometric accuracy. Theoretically, for a part that requires forming with a multi-pass ISF process, there are infinite varieties of the designing of intermediate shapes. Liu et al. [14] proposed a systematic method of designing intermediate shapes. According to their research, the intermediate shapes can be parametrized by three basic geometric features, i.e., radius (applies to circular shapes only), wall angle, and depth, which are denoted as strategy A, B, and C, respectively, in the following context. More complex designs can be achieved by combining the three basic features. In this study, both of the two target parts were formed in three passes. And, based on the method proposed by Liu et al. [14], intermediate shapes were designed using the strategy B, B+C, and A+B+C, respectively. The strategies B and B+C can be applied to both parts, while the strategy A+B+C can be applied to the circular cone-shaped part only. Fig. 5 is the vertical view showing of the designed intermediate shapes, and the detailed geometric parameters can be found in Table 1.

2.5.2 Controller implementations and experimental apparatus

To assess the applicability and performances of the two developed MPC algorithms, a group of benchmark tests were conducted. Then, two additional groups of tests were carried out to further assess the generality of the algorithm with a better performance in the benchmark test.

In the benchmark tests, MPC-1 and MPC-2 were respectively used in forming the circular cone-shaped part using the intermediate shape design B. MPC-1 was activated in all the passes. The control problem for MPC-1 in the first pass was the same as that in the closed-loop single-pass ISF processes in our previous studies [16, 25]. In this situation, the depth of the bottom of the formed part was the dominant factor for the global geometric accuracy. More specifically, when the vertical error on the base was significantly compensated by optimizing the step-down trajectory, the horizontal error was largely reduced as well. As the target depths for all the intermediate shapes in design B were the same, in the benchmark test with MPC-1, the vertical module was enabled in the first pass to eliminate the majority of the global error caused by the springback on the bottom, while the remaining horizontal error was compensated in the following passes by the horizontal module. As MPC-2 was designed for compensating the

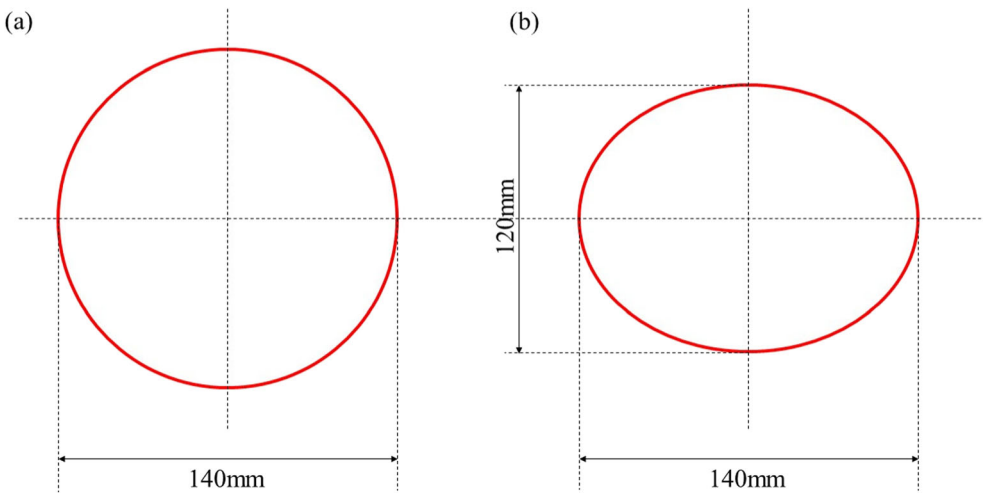

Fig. 4 Top view showings and dimensions of **a** a circular cone-shaped part and **b** an elliptical cone-shaped part.

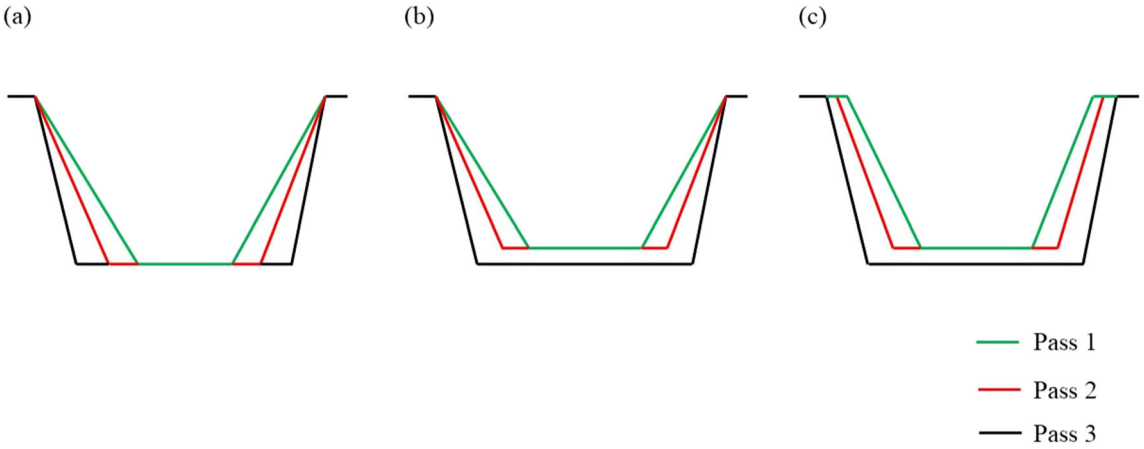

Fig. 5 Vertical view showing of the intermediate shapes of **a** design B, **b** design B+C, and **c** design A+B+C

geometric error in the final pass, it was activated in the final pass only, and nominal tool paths were used in previous passes. According to section 2.4, in the nominal steps of the final pass, the horizontal module was enabled to eliminate the horizontal error. Then, the fine control module was enabled to compensate the remaining vertical error iteratively. In the initial period of the single-point ISF process, the sloping wall cannot be formed to the full extent, and there is a transient area between the undeformed area and the wall [16, 26, 27]. Therefore, the scheduled control module was activated after the completion of first few steps. The scheme of the implementation of the controller is shown in Fig. 6.

In the second group of tests, the circular cone-shaped part in the benchmark test was used again, but with a different design of the intermediate shapes, i.e., design A+B+C. In the third group of tests, an elliptical cone-shaped part with the intermediate shape design B+C was formed. The controller implementation of the second and third groups of tests was the same as that in the benchmark test.

The multi-pass single-point ISF tests in this study were performed on a multi-axes computer-numerical-control (CNC) machine in the University of Queensland. Each test was performed once, and all the samples used in the tests were aluminum 7075 bare, with a size of 290*290mm and a thickness of 1.6mm. A tool with a round end was used in the tests and the diameter is 30mm. The nominal tool paths with 12 steps in each pass were planned by Siemens NX software. The controller was developed with Python 3.6 and was deployed on a Windows workstation. Detailed information about the apparatus can be found in [25]. The geometry of the partially or fully formed part was measured by a 3D scanner without unclamping, and the data format was cloud of points. The geometric error was obtained by comparing the clouds of points of the formed and the targeted geometry.

Table 1 Geometric parameters of the intermediate shape

Design	Pass	Geometric feature		
		Depth (mm)	Wall angle (deg)	Radius (mm)
B	1	30	47	N/A
	2	30	56	
	3	30	65	
B+C	1	29	47	N/A
	2	29	56	
	3	30	65	
A+B+C	1	28.5	49	69.5
	2	28.5	57	69.75
	3	30	65	70

3 Results and discussion

In this section, the results of the three groups of tests will be presented, and the applicability, performance, and generality of the two developed control algorithms will be analyzed and compared.

3.1 Test group 1—benchmark test

In the benchmark test, a circular cone-shaped part was formed in three passes, and the intermediate shapes were designed with the strategy B as explained in section 2.5.1. To assess the applicability and performances of the control algorithms, the benchmark part was formed with closed-loop multi-pass ISF processes that were controlled by MPC-1 and MPC-2, respectively. In addition, the part was formed with open-loop multi-pass and single-pass ISF, respectively, for comparison.

In the open-loop single-pass test, the forming process failed due to the occurrence of the crack, as shown in Fig. 7. This proved that for the target part, a multi-pass process is necessary.

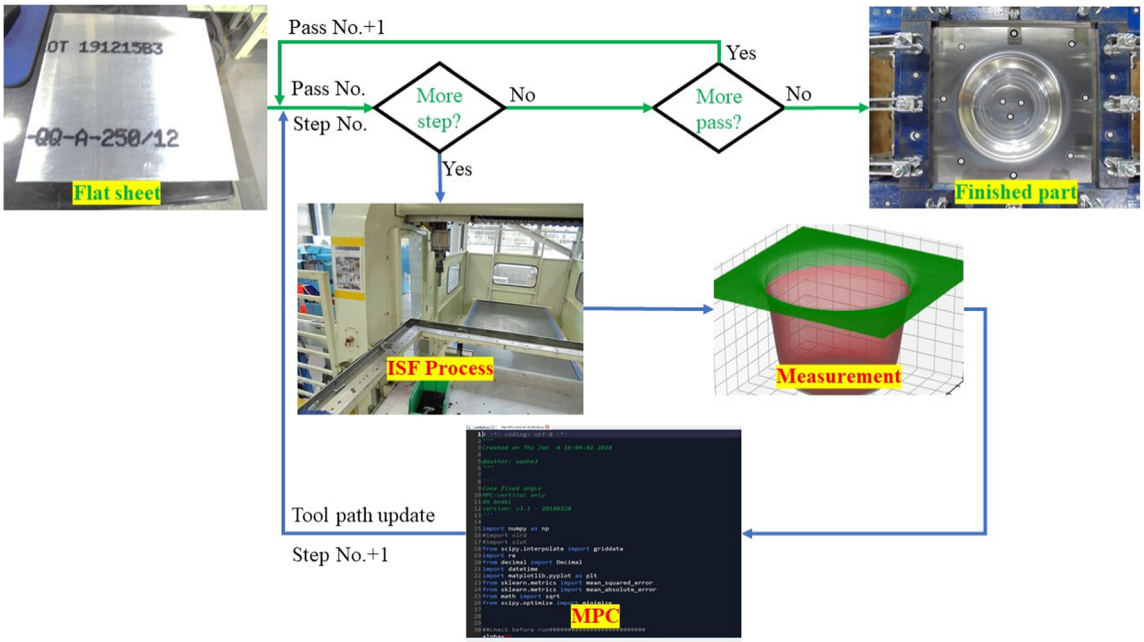

Fig. 6 Scheme of the implementation of the controller.

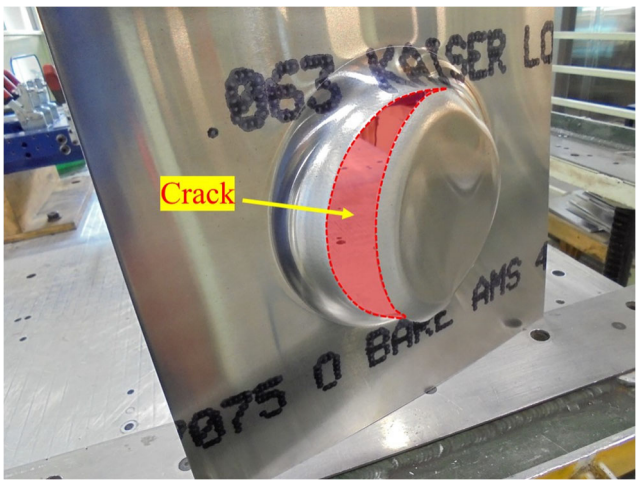

Fig. 7. Crack that occurred in the single-pass test of the circular cone-shaped part.

In the following multi-pass tests, the parts were formed successfully without cracks. In the open-loop test, the part was formed with the nominal tool paths for all the three passes. In the closed-loop tests, the parts were formed with the tool paths that were optimized by the MPCs. The trajectories of the control variables determined by MPC-1 and MPC-2 in the three passes are shown in Figs. 8, 9, and 10, respectively. Fig. 11 is the vertical view showing the formed part in the three passes. Fig. 12 shows the error distribution on the formed part. To further quantify the performances of the controller, the statistical analysis of the geometric error was carried out for different zones on the target part, as shown in Fig. 13. The detailed results of the statistical analysis are provided in Table 2.

It can be seen from Figs. 8, 9, and 10 that in pass 1 of the closed-loop process using MPC-1, the step-down trajectory was optimized by the vertical module after step 3, while the step-over kept unchanged. Fig. 11 a is the vertical view

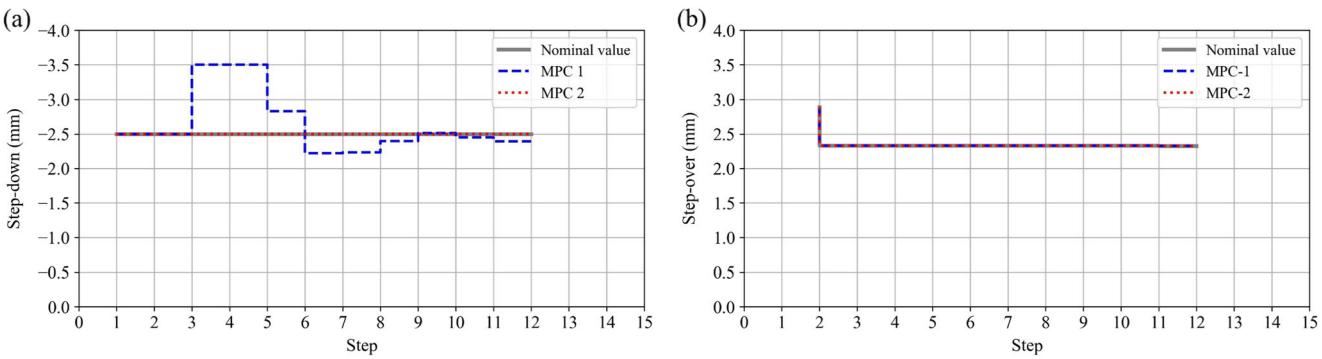

Fig. 8 Optimized trajectories of **a** step-down and **b** step-over of pass 1.

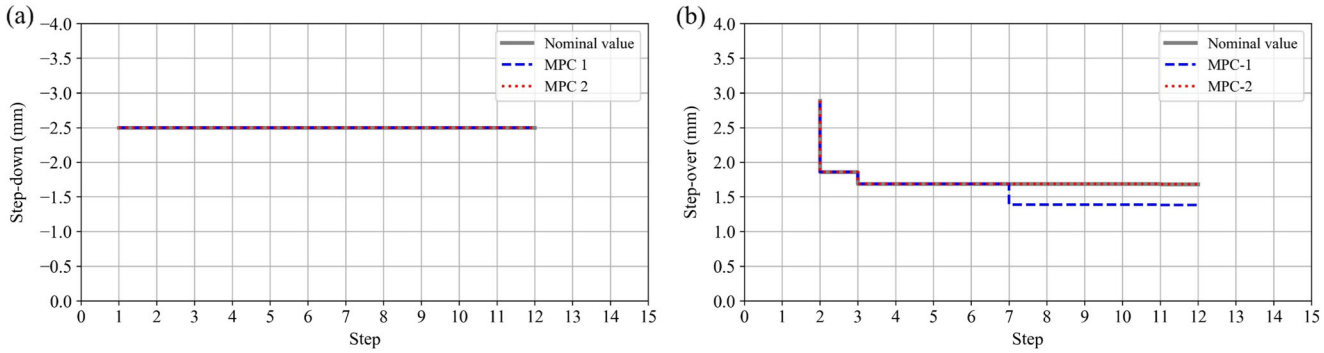

Fig. 9 Optimized trajectories of **a** step-down and **b** step-over of pass 2.

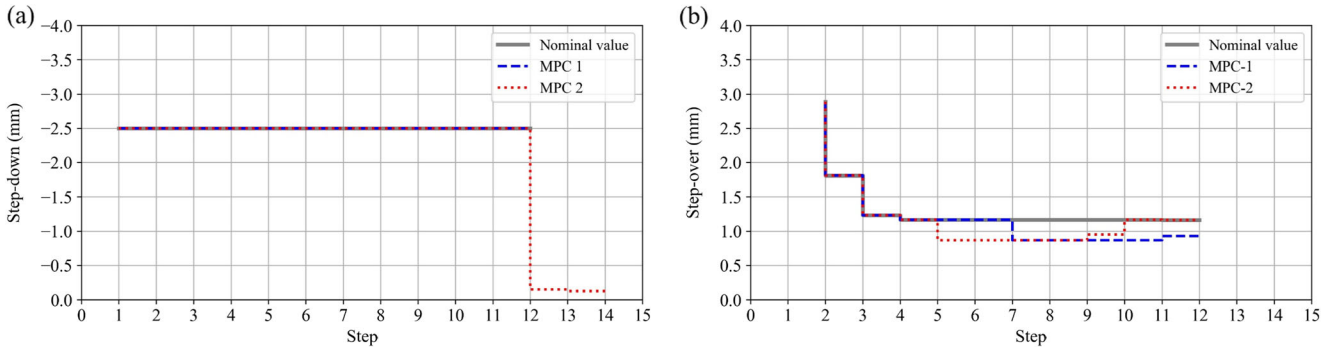

Fig. 10 Optimized trajectories of **a** step-down and **b** step-over of pass 3.

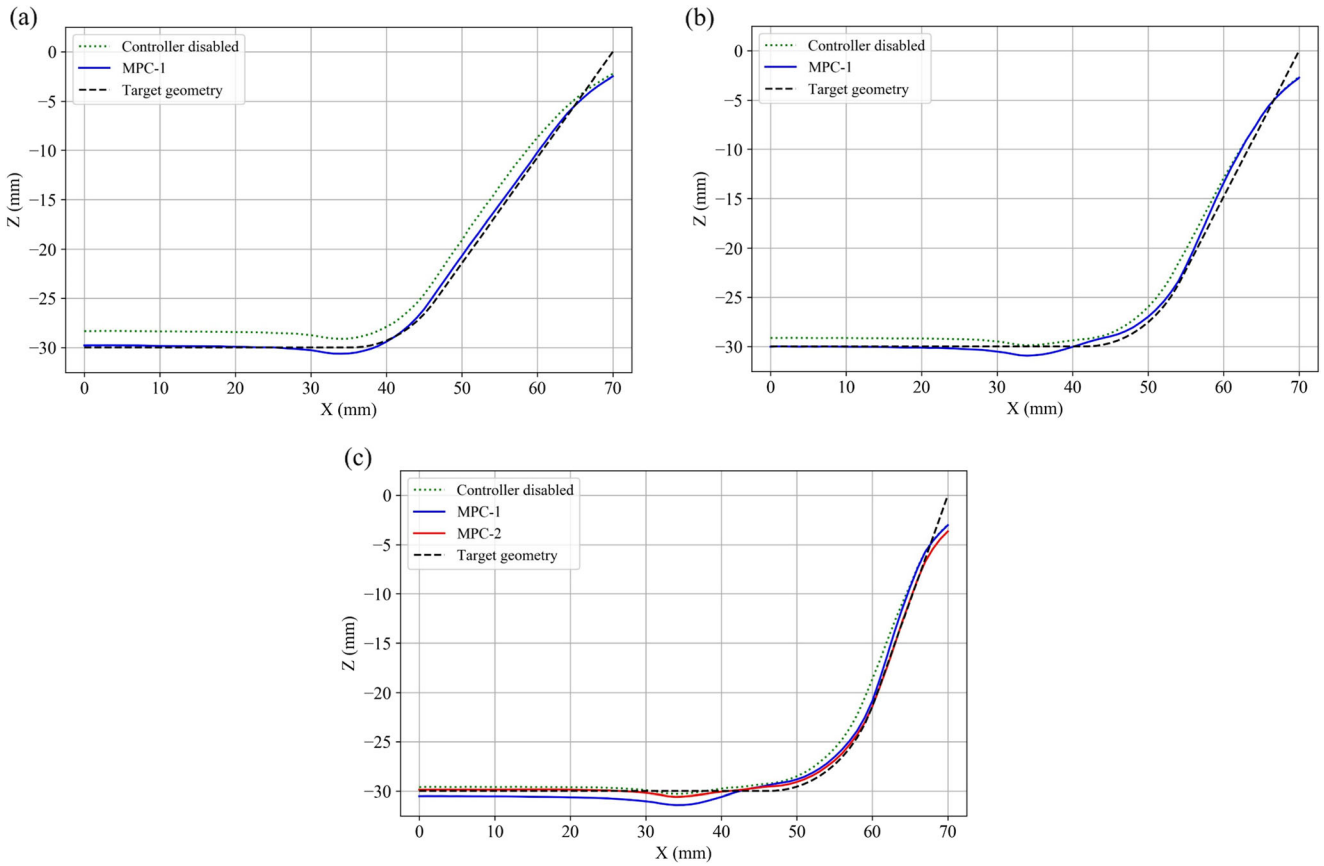

Fig. 11 Vertical view showings of the formed part in **a** pass 1, **b** pass 2, and **c** pass 3.

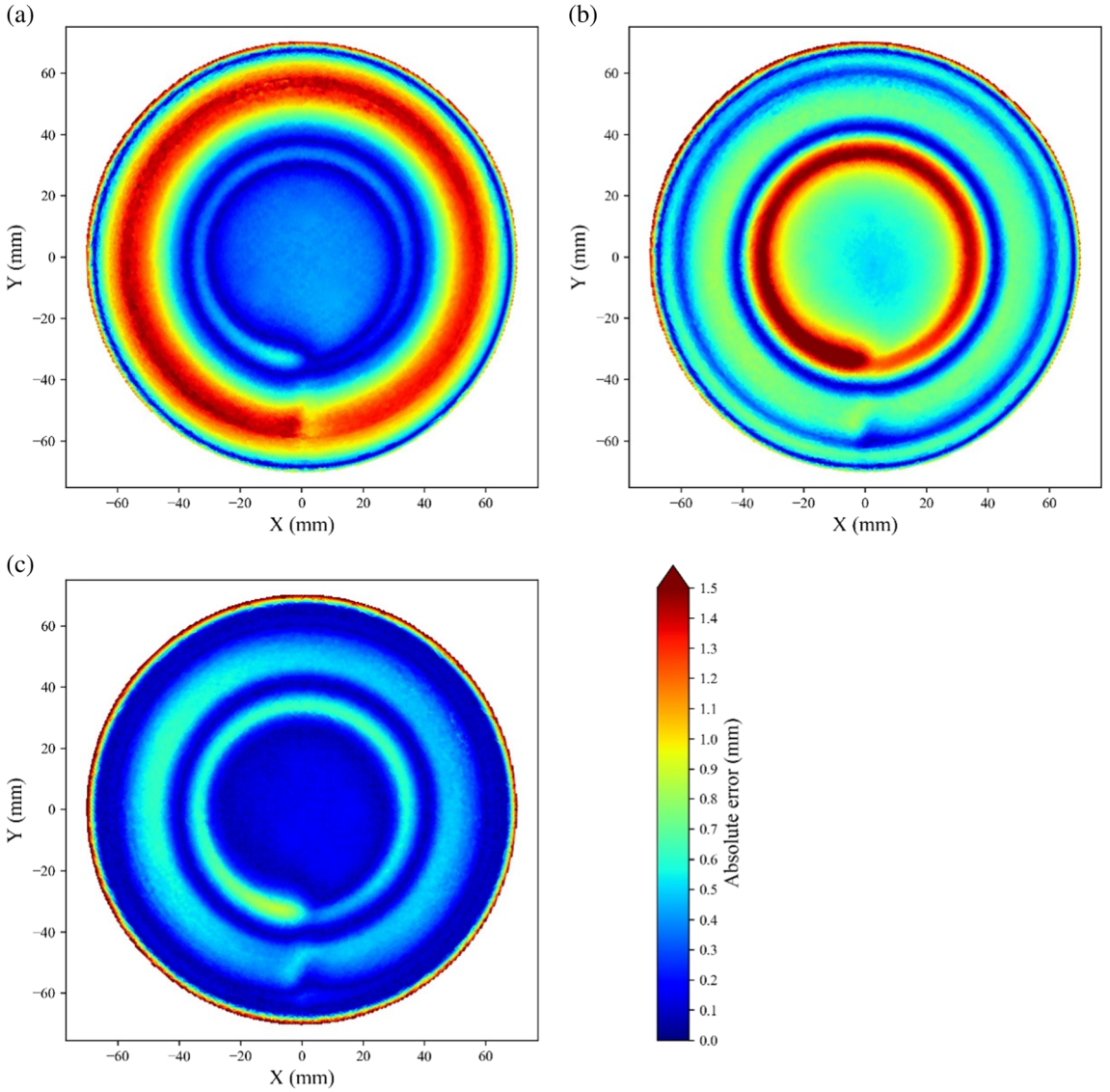

Fig. 12 Error distribution maps of the formed circular cone-shaped parts using multi-pass strategy B with **a** the controller disabled, **b** MPC-1, and **c** MPC-2.

showing of the formed part in pass 1, from which it can be seen that compared to the formed geometry in the open-loop process, both the vertical and the horizontal errors were reduced significantly by the vertical module. In passes 2 and 3, the step-down trajectories were kept unchanged, while the step-over trajectories after step 7 were optimized by the horizontal module. It should be noticed from Fig. 11 that, in pass 2, the base of the part was overly formed from the position where it was in pass 1. In pass 3, this occurred as well. The reason is that when forming passes 2 and 3, the tool contacted with a sloping wall, which made the existence of a vertical component of the forming force possible. It was the vertical component of the force that pushed down the entire part. This downward over-forming phenomenon can also be observed in the work of Liu et al. [14] in which the multi-pass ISF process was also employed; however, it does not exist in the authors' previous work [25] in which the single-pass ISF process was implemented. Due to the phenomenon described above, in the multi-pass ISF process, the individual passes were not independent. However, in MPC-1, the controller treated each pass as if they were independent single-passes, which made the MPC-1 unable to perform properly in the multi-pass ISF process. This phenomenon also happened in the closed-loop process with MPC-1, as shown in Fig.11, which deteriorated the achieved geometric accuracy in the base of the part. The maximum geometric error of the base achieved in the open-loop test was 0.45±0.04mm. However, in the closed-loop process with the MPC-1, the maximum base error was 0.75±0.04mm, which was even higher than the error in the open-loop test. Besides, compared to the open-loop test, MPC-1 enlarged the error in the conjunction zone from 1.17 ±0.04mm to 1.78±0.04mm. The statistical analysis

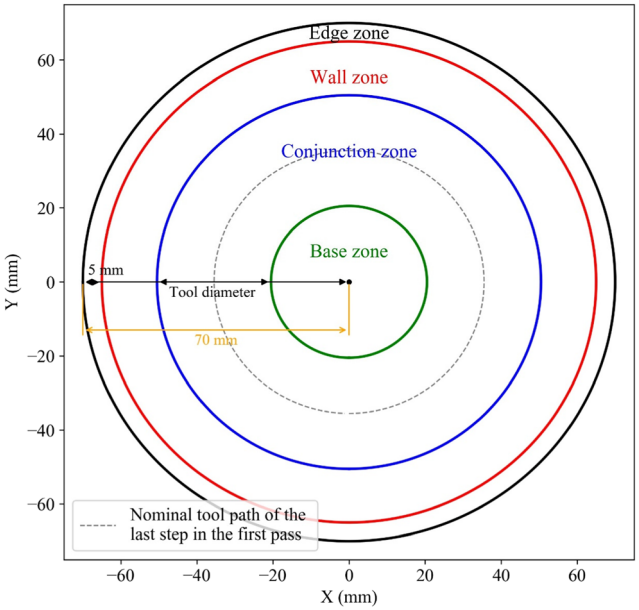

Fig. 13 Top view showings of different zones on the circular cone-shaped part.

further proved that the MPC-1 was not applicable to the multi-pass ISF process.

Considering the downward over-forming phenomenon in the multi-pass ISF process, MPC-2 was designed to be enabled in the last pass only. In MPC-2, the vertical control module was removed. In pass 3, the horizontal module optimized the step-over trajectory after step 5 of the nominal steps. When the nominal steps were completed, the maximum and the average error on the base were 0.26±0.04 and 0.19 ±0.04mm, respectively. Then, the base error was further compensated by the fine control module. The fine control module stopped in 2 iterations and reduced the maximum and the average error on the base to 0.20±0.04 and 0.14±0.04mm, respectively. As explained in section 2.2, to reduce the computational cost, the representative points were used to represent the geometry of the base. The stopping criterion of the fine control module was that the measured average vertical error of the vertical geometry representative points was smaller than 0.1mm. That was the reason why the average error on the entire base was slightly larger than the threshold. In addition, compared to the open-loop test, the MPC-2 reduced the maximum errors of the wall from 1.57±0.04 to 0.62±0.04mm, and reduced the maximum errors of the conjunction zone from 1.17 ±0.04 to 0.87±0.04mm. According to the previous study [7, 16, 22, 23, 25], the edge error cannot be compensated in single-point ISF, since there is no underneath support, and this was confirmed in this study.

Compared to MPC-1, MPC-2 reduced the maximum geometric error in the wall, conjunction, and base zones by 26%, 51%, and 73%, respectively. The comparison indicated that MPC-2 had a better performance in the multi-pass ISF process.

3.2 Test group 2—additional test

The benchmark test proved that MPC-1 was not applicable to the multi-pass ISF process, since it cannot handle the downward over-forming phenomenon properly. In contrast, MPC-2 performed well in the test. To further test the generality of the MPC-2, in this group of tests, the MPC-2 was used in forming the target part in the benchmark test again but with the intermediate shape design A+B+C. The multi-pass open-loop test with controller disabled was also performed for comparison. Fig. 14 shows the error distribution of the formed part. Compared to the open-loop test, in the closed-loop test with MPC-2, the maximum error in the wall and conjunction zones reduced from 1.67±0.04 to 1.03±0.04mm and 1.37±0.04 to 0.99±0.04mm, respectively. When the

Table 2 Results of the statistical analysis of the geometric errors of the circular cone-shaped part with the intermediate shape design B.

Zone	Statistical index	Controller disabled (±0.04, mm)	MPC-1 (±0.04, mm)	MPC-2 (±0.04, mm)
Edge	Maximum	1.52	1.60	1.81
	Minimum	0.01	0.01	0.01
	Average	0.54	0.53	0.45
Wall	Maximum	1.57	0.84	0.62
	Minimum	0.57	0.02	0.00
	Average	1.17	0.50	0.20
Conjunction	Maximum	1.17	1.78	0.87
	Minimum	0.00	0.02	0.01
	Average	0.43	0.81	0.32
Base	Maximum	0.45	0.75	0.20
	Minimum	0.29	0.48	0.03
	Average	0.39	0.59	0.14

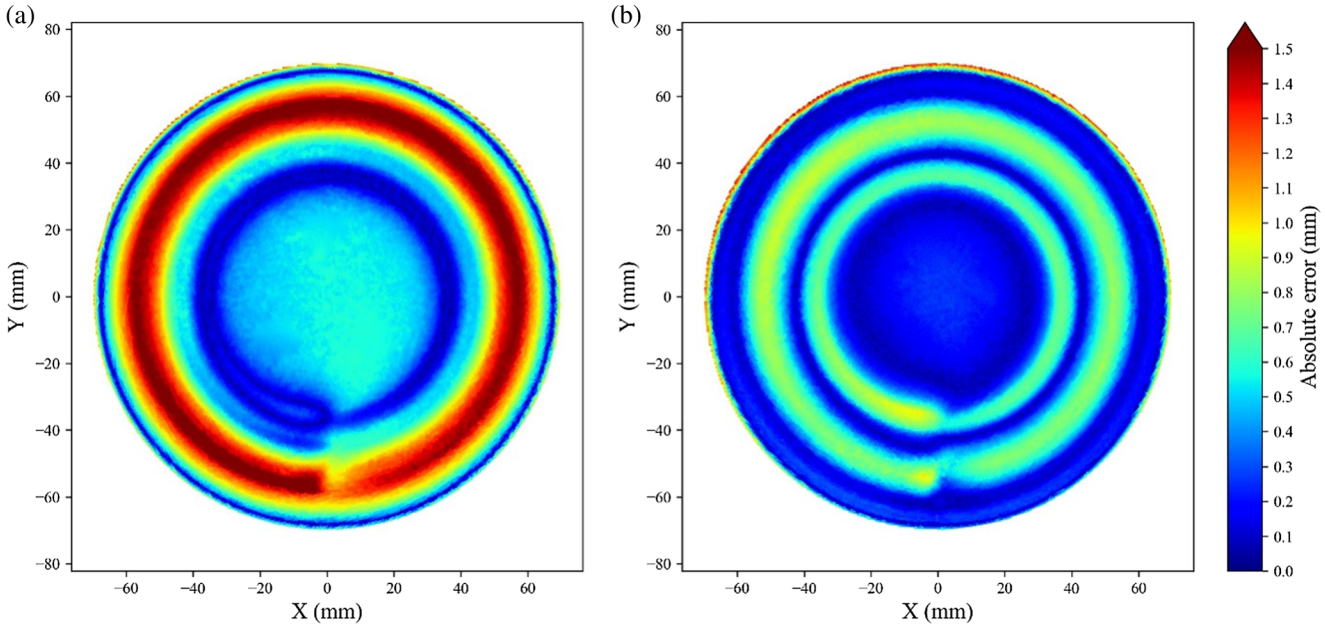

Fig. 14 Error distribution maps of the formed circular cone-shaped parts using multi-pass strategy A+B+C with **a** the controller disabled and **b** MPC-2.

nominal steps in the pass 3 of the closed-loop process were completed, the maximum error on the base was 0.65±0.04mm, and the fine control module reduced the error to 0.30±0.04mm in 4 iterations. The archived maximum error on the base was far less than that obtained in the open-loop test, i.e,. 0.61±0.04mm.

3.3 Test group 3—additional test

In the third group of tests, an elliptical cone-shaped part was formed with the open-loop process and the closed-loop process controlled by MPC-2. The used strategy of the intermediate shape design was B+C. Fig. 15 shows the error distribution of the formed part, and Fig. 16 shows the different zones on the part that were defined for the statistical analysis. The maximum errors in the wall and the conjunction zones were reduced from 1.68±0.04 to 0.90±0.04mm and 1.38±0.04 to 0.91±0.04mm by MPC-2, compared to the open-loop test. The maximum base error achieved in the last nominal step in the final pass was 0.61±0.04mm, and it was reduced to 0.25 ±0.04mm by the fine control module. The maximum base error obtained in the open-loop test was 0.57±0.04mm.

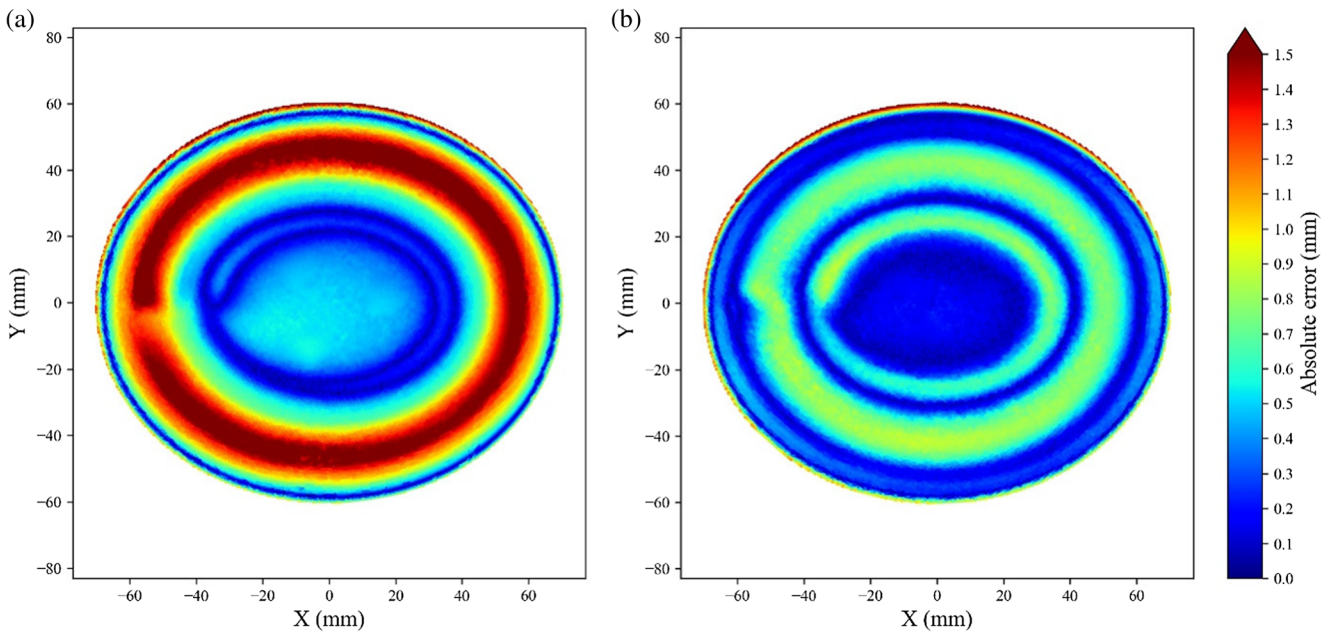

Fig. 15 Error distribution maps of the formed elliptical cone-shaped parts using multi-pass strategy B+C with **a** the controller disabled and **b** MPC-2.

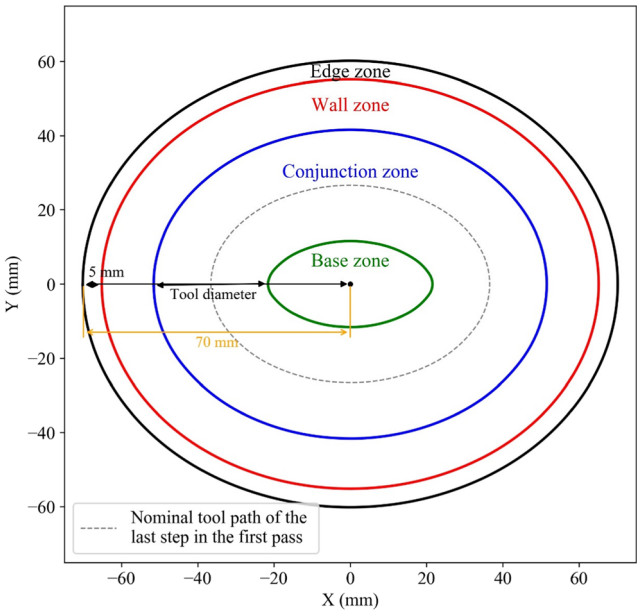

Fig. 16 Top view showings of different zones on the elliptical cone-shaped part.

The results of the additional tests show that the MPC-2 can be applied to various target geometries and various intermediate shapes, which confirmed the generality of the control algorithm.

4 Conclusion

In this study, for the first time, the on-line autonomous path optimization approach for multi-pass ISF processes was proposed, developed, and validated. Two model predictive path control algorithms were formulated. MPC-1 was designed to be activated in all the passes and treated each pass independently, which was composed of a vertical control module and a horizontal control module. MPC-2 was designed to eliminate the errors raised in the entire process in the final pass, and it contained a horizontal control module and a fine control module.

The benchmark tests were conducted by forming a circular cone-shaped part in three passes with the intermediate shape design B using the two MPCs. The maximum errors achieved on the wall were 1.57±0.04, 0.84±0.04, and 0.62±0.04mm with the controller disabled, MPC-1, and MPC-2, respectively. Those achieved in the conjunction zone were 1.17±0.04, 1.78±0.04, and 0.87±0.04mm with the controller disabled, MPC-1, and MPC-2, respectively. The maximum error on the base was 0.45±0.04mm in the open-loop process without the controller, and it was 0.75±0.04 and 0.20±0.04mm in the closed-loop process with MPC-1 and MPC-2, respectively. MPC-2 reduced the maximum geometric error in the wall, conjunction, and base zones by 26%, 51%, and 73%, respectively, compared to MPC-1. The results show that MPC-1 cannot handle the downward over-forming phenomenon on the base and thus is not applicable to the multi-pass ISF process. In contrast, MPC-2 achieved a desired performance.

Two additional tests were carried out to further prove the generality of MPC-2. In the first additional test, the part in the benchmark test was formed with another intermediate shape design, i.e., A+B+C. Compared to the open-loop test, the maximum geometric error in the closed-loop process was reduced from 1.67±0.04 to 1.03±0.04mm (by 38%), 1.37±0.04 to 0.99±0.04mm (by 28%), and 0.61±0.04 to 0.30±0.04mm (by 51%) in the wall, conjunction, and base zones, respectively. In the second additional test, an elliptical cone-shaped part was formed with the intermediate shape design B+C. Compared to the open-loop process, MPC-2 reduced the maximum error on the wall from 1.68±0.04 to 0.90±0.04 mm (by 46%), in the conjunction zone from 1.38±0.04 to 0.91 ±0.04mm (by 34%), and on the base from 0.57±0.04 to 0.25 ±0.04mm (by 56%). MPC-2 was tested in forming different parts using different intermediate shapes in three groups of tests, which proved that MPC-2 had a good performance and wide generality in forming parts with single-point multi-pass ISF processes. Future works will be focusing on implementations of the developed algorithm on manufacturing parts with more complex geometric features and extending the present algorithm to multi-point multi-pass ISF processes.

Funding The authors acknowledge Queensland Government, Boeing Research & Technology - Australia, The University of Queensland, and QMI Solutions for the support and collaboration through the Advanced Queensland Innovation Partnerships Project 2016000418. The first author acknowledges the University of Queensland for financial support.

Data availability The data is not available.

Code availability The code is not available.

Declarations

Conflict of interest The authors declare no competing interests.

References

1. Lu H, Liu H, Wang C (2019) Review on strategies for geometric accuracy improvement in incremental sheet forming. Int J Adv Manuf Technol 102(9-12):3381–3417. https://doi.org/10.1007/s00170-019-03348-3
2. Meier H, Buff B, Laurischkat R, Smukala V (2009) Increasing the part accuracy in dieless robot-based incremental sheet metal forming. CIRP Ann 58(1):233–238. https://doi.org/10.1016/j.cirp.2009.03.056
3. Mohanty S, Regalla SP, Daseswara Rao YV (2019) Robot-assisted incremental sheet metal forming under the different forming condition. J Braz Soc Mech Sci Eng 41(2). https://doi.org/10.1007/s40430-019-1581-6

4. Störkle DD, Möllensiep D, Thyssen L, Kuhlenkötter B (2018) Geometry-dependent parameterization of local support in robot-based incremental sheet forming. Procedia Manuf 15:1164–1169. https://doi.org/10.1016/j.promfg.2018.07.373
5. Li Y, Chen X, Zhai W, Wang L, Li J, Guoqun Z (2018) Effects of process parameters on thickness thinning and mechanical properties of the formed parts in incremental sheet forming. Int J Adv Manuf Technol 98(9-12):3071–3080. https://doi.org/10.1007/s00170-018-2469-9
6. Liu Z, Daniel WJT, Li Y, Liu S, Meehan PA (2014) Multi-pass deformation design for incremental sheet forming: analytical modeling, finite element analysis and experimental validation. J Mater Process Technol 214(3):620–634. https://doi.org/10.1016/j.jmatprotec.2013.11.010
7. Lu H, Kearney M, Li Y, Liu S, Daniel WJT, Meehan PA (2015) Model predictive control of incremental sheet forming for geometric accuracy improvement. Int J Adv Manuf Technol 82(9-12):1781–1794. https://doi.org/10.1007/s00170-015-7431-5
8. Li Y, Chen X, Liu Z, Sun J, Li F, Li J, Zhao G (2017) A review on the recent development of incremental sheet-forming process. Int J Adv Manuf Technol 92(5-8):2439–2462. https://doi.org/10.1007/s00170-017-0251-z
9. Liu F et al (2020) Modelling of the effects of process parameters on energy consumption for incremental sheet forming process. J Clean Prod 250. https://doi.org/10.1016/j.jclepro.2019.119456
10. Duflou JR et al (2008) Process window enhancement for single point incremental forming through multi-step toolpaths. CIRP Ann 57(1):253–256, 2008/01/01/. https://doi.org/10.1016/j.cirp.2008.03.030
11. Liu Z, Li Y, Meehan PA (2014) Tool path strategies and deformation analysis in multi-pass incremental sheet forming process. Int J Adv Manuf Technol 75(1-4):395–409. https://doi.org/10.1007/s00170-014-6143-6
12. Kim TJ, Yang DY (2000) Improvement of formability for the incremental sheet metal forming process. Int J Mech Sci 42(7):1271–1286. https://doi.org/10.1016/s0020-7403(99)00047-8
13. Skjoedt M, Silva MB, Martins PAF, Bay N (2009) Strategies and limits in multi-stage single-point incremental forming. J Strain Anal Eng Des 45(1):33–44. https://doi.org/10.1243/03093247jsa574
14. Liu Z, Li Y, Meehan PA (2013) Vertical wall formation and material flow control for incremental sheet forming by revisiting multi-stage deformation path strategies. Mater Manuf Process 28(5):562–571. https://doi.org/10.1080/10426914.2013.763964
15. Junchao L, Junjian S, Bin W (2013) A multipass incremental sheet forming strategy of a car taillight bracket. Int J Adv Manuf Technol 69(9):2229–2236, 2013/12/01. https://doi.org/10.1007/s00170-013-5179-3
16. He A, Kearney MP, Weegink KJ, Wang C, Liu S, Meehan PA (2020) A model predictive path control algorithm of single-point incremental forming for non-convex shapes. Int J Adv Manuf Technol. https://doi.org/10.1007/s00170-020-04989-5
17. Hirt G, Ames J, Bambach M, Kopp R, Kopp R (2004) Forming strategies and process modelling for CNC incremental sheet forming. CIRP Ann 53(1):203–206. https://doi.org/10.1016/s0007-8506(07)60679-9
18. Fu Z, Mo J, Han F, Gong P (2012) Tool path correction algorithm for single-point incremental forming of sheet metal. Int J Adv Manuf Technol 64(9-12):1239–1248. https://doi.org/10.1007/s00170-012-4082-7
19. Fiorentino A, Feriti GC, Giardini C, Ceretti E (2015) Part precision improvement in incremental sheet forming of not axisymmetric parts using an artificial cognitive system. J Manuf Syst 35:215–222. https://doi.org/10.1016/j.jmsy.2015.02.003
20. Fiorentino A, Giardini C, Ceretti E (2015) Application of artificial cognitive system to incremental sheet forming machine tools for part precision improvement. Precis Eng 39:167–172. https://doi.org/10.1016/j.precisioneng.2014.08.005
21. Mayne DQ, Rawlings JB, Rao CV, Scokaert POM (2000) Constrained model predictive control: stability and optimality. Automatica 36(6):789–814. https://doi.org/10.1016/s0005-1098(99)00214-9
22. Wang H, Duncan S (2011) Constrained model predictive control of an incremental sheet forming process. 2011 IEEE International Conference on Control Applications (CCA), 1288–1293
23. Lu H, Kearney M, Liu S, Daniel WJT, Meehan PA (2016) Two-directional toolpath correction in single-point incremental forming using model predictive control. Int J Adv Manuf Technol 91(1-4):91–106. https://doi.org/10.1007/s00170-016-9672-3
24. Lu H, Kearney M, Wang C, Liu S, Meehan PA (2017) Part accuracy improvement in two point incremental forming with a partial die using a model predictive control algorithm. Precis Eng 49:179–188. https://doi.org/10.1016/j.precisioneng.2017.02.006
25. He A, Wang C, Liu S, Meehan PA (2020) Switched model predictive path control of incremental sheet forming for parts with varying wall angles. J Manuf Process 53:342–355, 2020/05/01/. https://doi.org/10.1016/j.jmapro.2020.02.012
26. Allwood JM, Music O, Raithathna A, Duncan SR (2009) Closed-loop feedback control of product properties in flexible metal forming processes with mobile tools. CIRP Ann 58(1):287–290. https://doi.org/10.1016/j.cirp.2009.03.065
27. Bambach M (2010) A geometrical model of the kinematics of incremental sheet forming for the prediction of membrane strains and sheet thickness. J Mater Process Technol 210(12):1562–1573. https://doi.org/10.1016/j.jmatprotec.2010.05.003